ARTICLE

TECHNOLOGY

# Focal blood-brain-barrier disruption with high-frequency pulsed electric fields

**Christopher B. Arena[1,2,*], Paulo A. Garcia[1,3,*], Michael B. Sano[1,*], John D. Olson[4], Thomas Rogers-Cotrone[5], John H. Rossmeisl Jr.[5] & Rafael V. Davalos[1]**

**The blood-brain-barrier (BBB), a network of tight junctions that impedes large molecule transport, limits the usefulness of systemic chemotherapeutic delivery for the treatment of malignant gliomas and other neurological diseases. Here, we present a tool for BBB disruption that uses bursts of sub-microsecond bipolar pulses to enhance the transfer of large molecules to the brain. Blunt needle electrodes were advanced into the *motor cortex* of anesthetized adult rats, and a series of 90–900 bursts were delivered with voltage-to-distance ratios of 250 or 2000 V/cm, a total programmed energized time of 100 μs, and a repetition rate of 1 Hz. BBB disruption was assessed via a gadolinium-Evans blue albumin tracer, and all experimental conditions were found to cause BBB disruption immediately following treatment without inducing local or distal muscle contractions. The lowest energy condition, 300 bursts consisting of 850 ns bipolar pulses, resulted in significant BBB disruption (0.51 cm$^3$), without displaying necrotic or apoptotic damage to neurological tissue.**



## INNOVATION

The Vascular Enabled Integrated Nanosecond pulse (VEIN pulse) platform is a new technology for reversibly opening the blood-brain-barrier (BBB) to facilitate the treatment of brain cancer. Our experiments reveal that the delivery of bipolar sub-microsecond pulses eliminates the electrically induced movement associated with longer duration unipolar pulses used in irreversible electroporation and electrochemotherapy treatments. Therefore, it may be possible in the future to perform these procedures while patients are under conscious sedation and assess cognitive function as the therapy is being delivered. The sub-lethal nature of these bursts indicates that this modality may be useful for treating other neurological disorders, such as Parkinson's disease and epilepsy, in which certain therapeutics show effectiveness in *in vitro* models of disease, but fail to reach their therapeutic target *in vivo*. Generation of these waveforms is possible using solid-state electronics, enabling the creation of compact systems that can easily be scaled for human clinical applications.

## INTRODUCTION

Currently, there is no effective therapy for malignant glioma. By nature of their neuro-invasiveness, high-grade variants of gliomas are difficult to treat and generally considered incurable with singular or multimodal therapies[1–4]. One reason for poor survival is that treatment may be limited by inefficient intracellular delivery of chemotherapy. Most agents demonstrating *in vitro* cytotoxic effects against glial tumors do not cross the blood-brain-barrier (BBB) *in vivo*. Although the BBB is compromised in portions of high-grade gliomas that are associated with leaky blood vessels, there is evidence that these heterogeneous tumors contain areas of infiltrative tumor with an intact BBB that limits the effectiveness of systemic chemotherapeutics[5,6].

Techniques that uniformly increase BBB permeability and delivery of low-dose cytotoxic agents into tumors may yield improved tumor control[7,8]. Conventional osmotic agents or receptor-mediated mechanisms of BBB disruption result in widespread, non-targeted effects that can be associated with adverse events[9]. For example, when a bradykinin analog was used to disrupt the BBB in a Phase II trial for childhood brain tumors, the chosen dosage did not improve chemotherapeutic efficacy, and the patients experienced frequent headaches, flushing, and vomiting due to bradykinin[10]. Alternatively, focused ultrasound has emerged as a physical method to temporarily open the BBB[11]. The procedure involves systemic injection of gas filled microbubbles and transcranial delivery of acoustic energy focused at the target tissue[12]. It is thought that ultrasound induces oscillations in the microbubbles that safely open tight junctions in the blood vessel walls through mechanical stretching. Despite the non-invasive nature of the procedure, beam focusing reduces the coverage area of individual treatments, resulting in extended treatment times for large volumes[13].

Here, we investigate an alternative to chemical and acoustic modalities that utilizes electric fields. Previously, it was discovered that a series of short duration (~100 μs) high amplitude (~1000 V/cm) unipolar electric pulses could induce irreversible electroporation (IRE) of cell membranes without causing significant thermal effects[14,15]. This technology was

[1]Bioelectromechanical Systems Lab, School of Biomedical Engineering and Sciences, Virginia Tech-Wake Forest University, Blacksburg, VA, USA. [2]Laboratory for Ultrasound Contrast Agent Research, University of North Carolina — North Carolina State University, Joint Department of Biomedical Engineering, Chapel Hill, NC, USA. [3]Laboratory for Energy and Microsystems Innovation (LEMI), Massachusetts Institute of Technology, Cambridge, MA, USA. [4]Center for Biomolecular Imaging, Wake Forest University School of Medicine, Winston-Salem, NC, USA. [5]Neurology and Neurosurgery, Virginia-Maryland Regional College of Veterinary Medicine, Blacksburg, VA, USA. *These authors contributed equally to this work. Correspondence should be addressed to M.B.S. (sano@vt.edu) and J.H.R. (jrossmei@vt.edu).

Received 13 April 2014; accepted 3 June 2014; published online 22 July 2014; doi:10.1142/S2339547814500186

successfully adapted for non-thermal tumor ablation, including malignant glioma[16,17]. Minimally invasive needle electrodes were inserted through a defect in the skull to direct the pulse application. While investigating the effects of IRE on brain tissue, it was revealed that sub-lethal pulse parameters resulted in transient disruption of the BBB due to reversible electroporation[18,19].

One challenge with delivering unipolar electric pulses for non-thermal ablation or BBB disruption is that they result in significant muscle contractions[20]. As electrically induced movement could compromise electrode positioning, IRE procedures typically require that patients receive a neuromuscular blocker and general anesthesia. Preliminary studies suggest that this requirement may be removed by designing pulses that alternate in polarity. When bipolar bursts of pulses with individual durations of 2 µs or less were applied to the sensorimotor cortex of rats, it was noted that non-thermal ablation could be achieved without inducing muscle contractions[21]. To the best of our knowledge, these types of pulses have not been studied *in vivo* for BBB disruption.

In this study, a custom pulse generator capable of delivering bipolar bursts of pulses as short as 500 ns was used to explore if sub-lethal BBB disruption can be achieved without causing muscle contractions. These Vascular Enabled Integrated Nanosecond (VEIN) pulse treatments were performed in normal rat brain by varying the pulse duration within a burst, the total number of bursts, and the applied field. BBB disruption was assessed using an Evans blue-albumin (EBA) complex uptake on histological sections and a gadolinium-EBA complex uptake on MRI scans. Muscle contractions were monitored visually and with an accelerometer placed along the dorsum. Applying 300 bursts containing pulses of 850 ns resulted in BBB disruption without any electrically induced muscle contractions or cell death. Therefore, this technique has the potential to be performed clinically under conscious sedation without neuromuscular blockade.

## METHODS

### Animals and intracranial VEIN pulse delivery procedure

All study procedures were approved by the Institutional Animal Care and Use Committee approval (10-163-CVM). Eighteen male Fischer 344 rats weighing 190–225 g were pre-medicated with buprenorphine (0.02 mg/kg subcutaneously) and then anesthetized with inhaled isofluorane delivered via induction chamber. Anesthesia was maintained with inhaled isofluorane delivered through a nose cone; provision of a surgical plane of anesthesia was assessed by loss of the tail or toe pinch reflex. A 3-axis accelerometer breakout board (Adafruit Industries ADXL335), capable of sensing muscle contractions up to 3 g and fitted with low-pass filter capacitors (0.1 µF) at the x, y, and z outputs for noise reduction, was secured to the dorsum of each rat at the cervicothoracic junction using 5-0 monocryl suture. The hair of the skull was clipped and aseptically prepared using povidone-iodine and alcohol solutions. Anesthetized rats were placed in a small animal stereotactic head frame (Model 1530M, David Kopf Instruments, CA, USA). A routine, right unilateral rostrotentorial surgical approach to the skull was made and a 1.5 mm × 5 mm rectangular craniectomy defect was created in the skull of each rat using a high-speed electrical drill. The rostral aspect of the craniectomy was created at the following stereotactic location relative to the bregma: 4 mm posterior and 3.5 mm lateral and extended caudally. The exposed dura was punctured with scalpel blade or hypodermic needle, and the electrodes were then advanced to a depth of 1.5 mm beneath the surface of dura using the manipulator arm of the stereotactic frame. The electrodes used for pulse delivery were blunt-tipped electrodes (0.45 mm Ø, 0.4 cm spacing, and 1.0 mm exposure) as previously described[18].

The pulse parameters delivered to rodents are summarized in **Table 1**. The applied voltage-to-distance ratios across the 0.4 cm gap are used to define the electric field, even though it is understood that needle electrodes produce a non-uniform distribution. Waveforms were generated

**Table 1** Treatment group matrix for *in vivo* BBB disruption

| Group | Programmed pulse duration (µs) | Programmed voltage-to-distance (V/cm) | Number pulses per burst | Number bursts |
|---|---|---|---|---|
| 1 ($n = 3$) | 0.5 | 250 | 200 | 300 |
| 2 ($n = 3$) | 0.5 | 250 | 200 | 600 |
| 3 ($n = 4$) | 0.5 | 250 | 200 | 900 |
| 4 ($n = 3$) | 2 | 250 | 50 | 900 |
| 5 ($n = 2$) | 0.5 | 2000 | 200 | 90 |
| 6 ($n = 3$) | 0 | 0 | 0 | 0 (Sham, $n = 2$ or unoperated control, $n = 1$) |

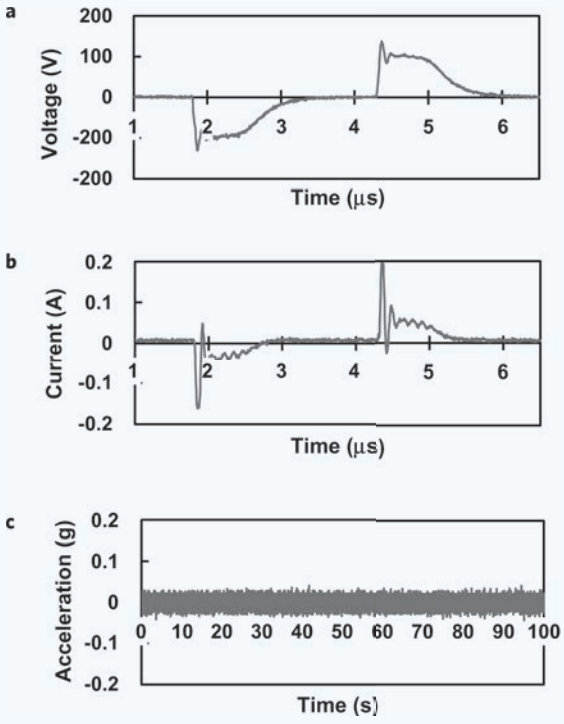


**Figure 1** VEIN pulse example output and accelerometer recording. (**a**) Voltage recording during 2 of the 200 pulses that comprised a single burst from a Group 3 treatment. (**b**) The corresponding current measurement. (**c**) The corresponding acceleration measurement (reported as normalized g-force).

using an arbitrary function generator (AFG3011, Tektronix Inc., Beaverton, Oregon) to trigger a custom-built high voltage pulse generator capable of delivering ± 1000 V (Applied Energetics, Tucson, AZ, USA). Output waveforms were visualized using an oscilloscope (TDS1002b, Tektronix Inc., Beaverton, Oregon) paired with a 50 MHz, 1000× high voltage probe (P5210A, Tektronix Inc., Beaverton, Oregon) and a 50 MHz clamp on current probe (TCP305A, Tektronix Inc., Beaverton, Oregon). Short circuit protection resistors on the output limited our maximum output voltage to approximately 800 V (2000 V/cm). An example waveform from Group 2 is shown in **Fig. 1**. In each trial, the bursts were applied once per second, and the burst on-time was held constant (100 µs) by varying the number of pulses within each burst (i.e., shorter pulse durations require more pulses to achieve the desired on-time). Data from the experiments was analyzed

using MATLAB (Version R2013a, The MathWorks Inc., Natick, MA). An algorithm was used to calculate the average amplitude of the pulses. Then, time points corresponding to one half of the pulse amplitude were found, and the pulse width was calculated as the full width at half maximum.

In all rats, 5 minutes prior to delivery of the pulses, 2.5 ml of 2.5% Evans blue solution was delivered via intraperitoneal injection and bound to albumin in the blood (67 kDa) to form the EBA complex[22]. Select rats subjected to MRI examinations received 2.5 ml of gadolinium-EBA (Gd-EBA) solution (74 kDa). Both formulations are considered high molecular weight tracers designed to mimic the diffusion properties of polar protein drugs (growth factors, antibodies, genetic vectors). The Gd-EBA solution was prepared by diluting a stock solution of 25 mg/ml Gd-albumin (Galbumin, BioPAL Inc., Worcester, MA, USA), containing 10–15 Gd-DTPA per albumin molecule, with deionized water to a concentration of 10 mg/ml. The Gd-albumin was then mixed with EB (1 mg Evans Blue (Sigma, St. Louis, MO, USA) per 2 ml Gd-albumin) to make the tagged Gd-EBA complex. Following completion of the pulse delivery, 15 minutes were allowed to lapse prior to withdrawal of the electrodes from the brain. Following removal of the electrodes, rats were euthanatized by intraperitoneal injection of 1 mL of phenytoin-pentobarbital solution (Beuthanasia-D, Abbott Laboratories, Abbott Park, IL, USA) followed by cervical dislocation. The brains were harvested and processed as described below.

### *Ex vivo* brain magnetic resonance imaging (MRI) examinations

Select rats which received IP Gd-EBA were subjected to *ex vivo* MRI examination of the brain *in situ* within 15 minutes of euthanasia using a 1.5-T superconducting magnet (Philips Intera, Philips Healthcare, Andover, MA, USA) with an 8-channel volume head coil. T1-weighted images were obtained in 3 planes using a spin echo sequence (Echo time [TE] = 15 ms, Repetition time [TR] = 410 ms, 2 mm slice thickness with 0.5 mm spacing, 224 × 224 mm field of view (FOV), and 256 × 256 mm matrix), and a high-resolution multiplanar three-dimensional gradient echo sequence (TE = 4.4 ms, TR = 25 ms, 1.5 mm slice thickness with no gap, 128 × 128 mm FOV, and 256 × 256 mm matrix).

Additional rodents receiving IP Gd-EBA underwent *ex vivo* MRI examination of the brain *in situ* within 2 hours of euthanasia using a 7.0-T small animal MRI scanner (Bruker Biospec 70/30, Ettlingen, Germany). A 38 mm inner diameter quadrature volume coil will be used for RF signal transmission and reception (Litzcage, Doty Scientific, Columbia, SC). Sequence acquisition parameters were: T1-weighted using a Rapid Acquisition with Relaxation Enhancement (RARE) pulse sequence with 8 echoes (TR = 1440 ms, TE = 7.5 ms, FOV = 4 cm, matrix = 256 × 256, slice thickness = 0.5 mm, NEX = 8), followed by T2-weighted using a RARE pulse sequence with 8 echoes (TR = 6575 ms, TE = 60 ms, FOV = 4 cm, matrix = 256 × 256, slice thickness = 0.5 mm, NEX = 8).

### Blood-brain barrier volumetric quantification and brain pathologic analyses

Following euthanasia, the brain was harvested and digital photographs were obtained of the dorsal surface of the entire brain prior to immersion fixation in 10% neutral buffered formalin solution. The immersion fixed intact brain of each rodent was inserted into an adult rodent matrix slicer (Zivix, Instruments, Pittsburg, PA, USA) and digital photographs obtained of the exposed dorsal surface of the brain. The brain was then serially sectioned in the transverse plane at 1 mm intervals extending from the olfactory bulbs to the rostral cerebellum, with each individual transverse section paraffin embedded in a tissue cassette. The positions of the transverse sections at which the Gd-EB was first and last visible (the anterior/rostral and posterior/caudal limits of the z-plane of the BBB disruption) were co-registered to the corresponding channels of the brain matrix and recorded. Transverse brain sections containing EBA within these defined rostral and caudal limits were serially sub-sectioned in the transverse plane at 10 μm thickness and 200 μm intervals using a microtome and mounted on charged microscope slides. Digital photomicrographs (Nikon Eclipse Ni-E, Nikon, Japan) of the fluorescent volumes intraparenchymal EBA were obtained from all intervening transverse sections using a charged-coupled device camera with a fixed aperture (Nikon DS-Fi1c, Nikon, Japan) and an ultraviolet light source. The volume of EBA fluorescence resulting from the transverse image stack from each rat was calculated using the volumetric algorithm on a commercial image analysis system (Stereo Investigator; MBF Bioscience, Williston, VT, USA).

### Caspase-3 immunohistochemistry

Transverse brain segments were sectioned at 5 μm and were dried at 37 °C for 1 hour. Deparaffinization and antigen retrieval were performed in Reveal solution in a decloaking chamber (Biocare Medical, Walnut Creek, CA, USA). Endogenous peroxidase activity was blocked by 30 minute incubation with 5% bovine serum albumin in PBS/0.2% TX-100 (Sigma, St. Louis, MO, USA), followed by two consecutive 10 minute washes in PBS (Sigma). Slides were then incubated overnight at room temperature with polyclonal primary antibody (ab4501, 1:200 dilution; Abcam, Cambridge, MA, USA). After washing twice for 10 minutes with PBS, slides were incubated with prediluted biotinylated goat anti-rabbit IgGs (Abcam) for 1 hour at room temperature and streptavidin horseradish-peroxidase (Vector, Burlingame, CA, USA). Immunoreactive cells were visualized with fast red chromogen and hematoxylin counterstain (Ventana Medical Syustems, Tucson, AZ, USA). Rat splenic tissue was used for a positive control, and negative controls were treated as described above save for omission of the primary antibody.

### Quantitative determination of caspase-3 immunoreactivity

Slides immunohistochemically stained for caspase-3 were examined by an investigator blinded to the experimental treatments. The specific slice examined in each rat was at the brain level containing the rostral electrode insertion track. The examiner was asked to select three 40× magnification random fields of view (RFV) from the following four brain regions of each rat from both the treated and contralateral untreated hemispheres of the brain: 1) the superficial cerebral cortex in the region of the electrode insertion, 2) the deep termination point of the electrode insertion, representing the electrode tip, 3) the hippocampal CA1 region in the treatment area, and 4) the choroid plexus of the lateral ventricle. The RFV from each region and hemisphere were captured with a charge-coupled device digital camera (Nikon DS-Fi1c). Digitized images were optically segmented, using intensity thresholding compared with positive control tissues, in order to allow discrimination of negative from positive (Nikon Elements AR, Nikon Japan). This segmentation process allowed for generation of binary images from which the number of positively stained objects and cell nuclei in each RFV could be quantified. For determination of labeling indices for each brain region, at least 500 total cells were counted, and a region-specific caspase-3 labeling index (LI) determined as follows:

$$\text{Caspase-3 LI} = \frac{\#\text{Caspase}-3\ \text{immunoreactive cells}}{\text{Total}\ \#\text{Nuclei}} \times 100 \qquad (1)$$

### Statistical analyses

One-way ANOVA was used to test for differences in the volume of BBB disruption between the VEIN pulse parameters tested, as well as to evaluate differences in caspase-3 LI among treatments and brain regions. When results of ANOVA were significant, Tukey post-hoc comparisons were used to examine differences among treatment groups. Statistical analyses were performed using commercial software (SAS, version 9.0, Cary, NC, USA) and $\alpha = 0.05$.

## RESULTS

### VEIN pulse intracranial procedure

Other than normal respiratory motions occurring under anesthesia, no gross movement was observed during VEIN pulse administration in any

rodent in the study, and no significant intraoperative complications were noted in any rodent. Additionally, the accelerometer was unable to detect any electrically induced movement (shown for Group 2 in **Fig. 1**). It is important to note that the accelerometer recordings from the high voltage trials (Group 5) were corrupted by electrical noise that fell within the same frequency bandwidth as a typical muscle contraction. This eliminated the possibility of filtering to isolate potential muscle contractions. In this case, visual observation served as the only means to assess muscle contractions, or lack thereof. **Figure 1** also includes samples of the voltage and current measurements from Group 2.

At low voltages, the shortest pulse duration achieved was, on average, 850 ns. The rise and fall times of these short duration pulses are dependent on the resistance and capacitance of the electrodes and tissue. A 500 ohm resistor was placed in parallel with the load to aid in waveform shaping. In the low voltage experiments, this technique was less successful in producing the desired wave shape. The waveform was slightly distorted with the pulses having an extended fall time. As the voltage increased, the pulse duration approached the desired mark of 500 ns per phase (**Table 2**). This decrease in pulse duration is likely due to electroporation effects decreasing the resistance of the tissue and, in turn, creating a shorter pulse fall time.

**Table 2** Energy and temperature calculations (values from Ref. 16 for comparison).

| Group | Measured pulse duration (μs) | Measured voltage-to-distance (V/cm) | Number bursts | Energy per treatment (J/m$^3$) | Predicted temperature change (°C) |
|---|---|---|---|---|---|
| 1 | 0.85 | 260 | 300 | $5.6 \times 10^6$ | 1.35 |
| 2 | 0.85 | 260 | 600 | $1.1 \times 10^7$ | 2.70 |
| 3 | 0.85 | 260 | 900 | $1.7 \times 10^7$ | 4.05 |
| 4 | 2.59 | 253 | 900 | $1.3 \times 10^7$ | 3.08 |
| 5 | 0.48 | 1995 | 90 | $6.1 \times 10^7$ | 14.62 |
| IRE* | 50 | 1250 | 80 | $1.1 \times 10^7$ | 2.64 |

* Ref. 16.

### VEIN pulse blood brain barrier disruption

Focal disruption of the BBB was achieved in all treated rodents as evidenced by the visualization of EBA or Gd-EBA solutions within treated brain regions on pathological or MRI examinations, and absence of tracer uptake in the sham operated controls and contralateral control hemispheres (**Fig. 2**). The treatment location is illustrated by **Fig. 2d**, where the white "x" marks indicate electrode positioning, and the broken line indicates the superficial region of BBB disruption as evidenced by EBA uptake. On select MRI scans (**Fig. 2b,c,d**), hyperintense areas signifying Gd uptake correspond with regions of EBA on pathologic sections. In the sham operated brain slice (**Fig. 2g**), hemorrhage within the electrode insertion track is visible.

The volume of BBB disruption differed significantly among the examined treatment parameters (ANOVA, $F(2,4) = 36.44$, $p = 0.0027$). Post-hoc comparisons (**Fig. 3**) indicated that the mean volume of BBB disruption was significantly smaller in Group 1 ($0.51 \pm 0.04$ cm$^3$) compared to all other groups, and significantly larger in Group 5 ($1.09 \pm 0.12$ cm$^3$) compared to all other groups. Volumes of BBB disruption did not differ significantly between Groups 2 ($0.68 \pm 0.03$ cm$^3$) and 3 ($0.68 \pm 0.09$ cm$^3$; $p = 0.73$), Groups 3 and 4 ($0.63 \pm 0.06$ cm$^3$; $p = 0.59$), or Groups 2 and 4 ($p = 0.48$).

### Histopathological analysis of VEIN pulse delivery

No microscopic or gross abnormalities were detected in unoperated contralateral control brains. In the treated cerebral hemispheres of Groups 1 and 6, lesions were limited to the physical displacement of the brain tissue in the trajectory of the electrode insertion, with occasional foci of hemorrhage noted on the pial surface or within the electrode track (**Fig. 4a,f**). In Groups 2, 3, and 4, the laminar organization of the brain remained intact, but there was mild vacuolization of the neuropil in regions of BBB disruption, as well as foci of neurons, glia, vascular endothelium, and choroid plexus epithelium demonstrating cytoplasmic condensation, nuclear pyknosis, and apoptotic body formation (**Fig. 4b–d**). The brains of Group 5 rats displayed severe cytoarchitectural disruption, perivascular inflammation, and coagulative brain necrosis in treated regions (**Fig. 4e**).

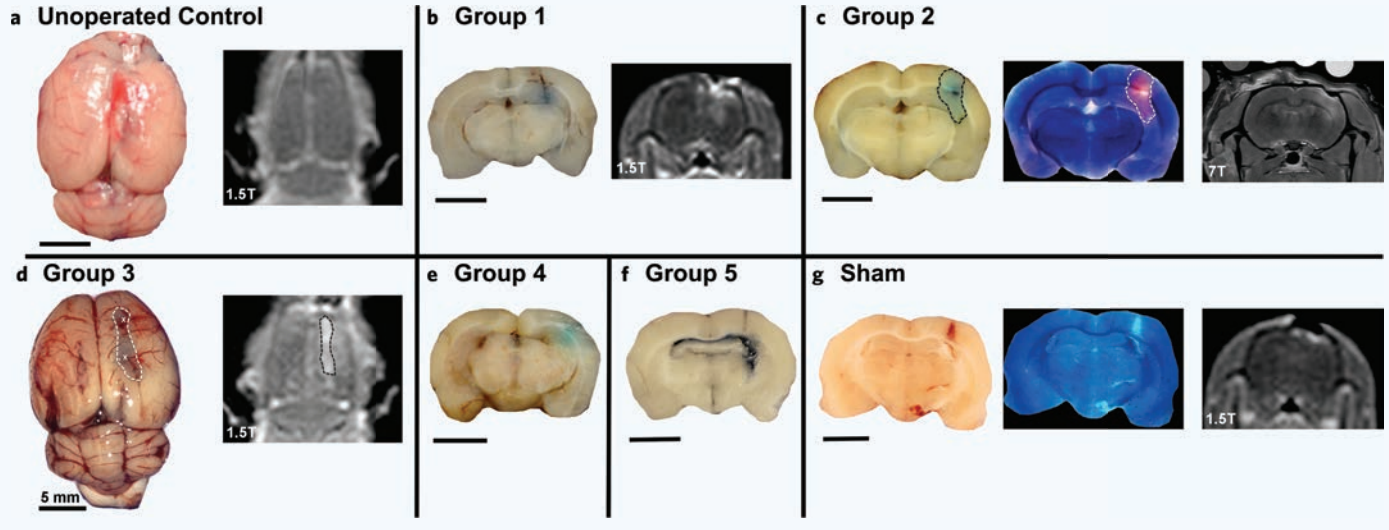


**Figure 2** Pathologic and MRI evidence of BBB disruption induced by VEIN pulses. All treatments were administered in the right cerebral hemispheres. The electrode insertion points (white "x" marks) relative to the dorsal surface of the brain (**d**) and limits of BBB disruption (broken line) are depicted in panels **c** and **d**. No evidence of Gd-EBA tracer uptake within the brain is visible in unoperated control (**a,** dorsal view) or sham operated brains (**g,** transverse view). In gross brain slice preparations, regions of BBB disruption are indicated by the uptake of the blue EBA within the parenchyma (**b,c,d,e,f**), or by the red region on segmented brain images (**c**). Areas of BBB disruption appear as hyperintense (white) areas on T1-weighted MRI examinations, and correspond with regions of EBA visualized in brain slices (**b,c,d**). Bar = 5 mm in all panels.

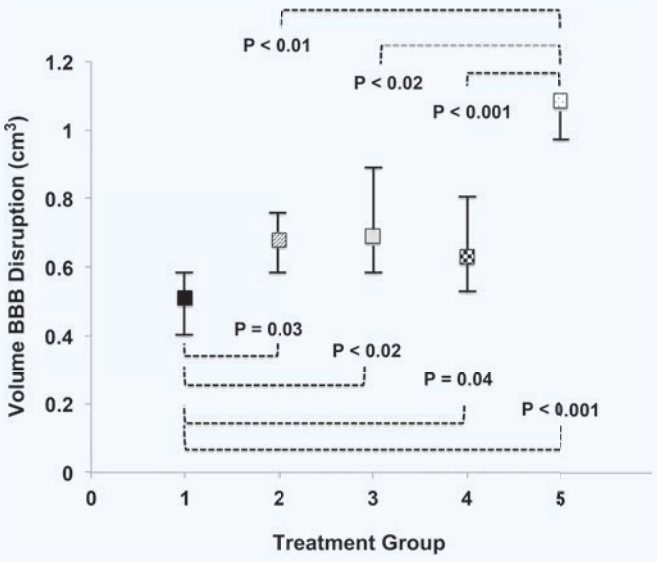


**Figure 3** Volumes of BBB disruption associated with VEIN pulse treatment parameters. The volume of BBB disruption was significantly less in Group 1 and significantly greater in Group 5 compared to all other groups.

### Caspase-3 immunohistochemistry

Group 3 caspase-3 LI was significantly ($p < 0.01$) higher than all other groups in each of the superficial cortical, deep cortical, and choroid plexus brain regions (**Figs. 5, 6**). Marked caspase-3 immunoreactivity was seen in the SC, DC and CP regions of Group 3 (**Fig. 5f,j,n**), with numerous caspase-3 immunoreactive neurons adjacent to the electrode insertion track in the DC region (**Fig. 5j**). The caspase-3 LI of groups 2, 4, and 5 were also observed to be significantly greater than sham operated or untreated controls in at least one area among the superficial cortical, deep cortical, and choroid plexus brain regions. There were no significant differences observed in the casapse-3 LI between Group 1, 6, or untreated control hemispheres for any of the 4 brain regions examined. No differences were noted between any group in the caspase-3 LI of the hippocampal CA1 region (**Fig. 6a**).

## DISCUSSION

Sub-lethal BBB disruption was achieved immediately following treatment at the lowest energy setting (Group 1), which consisted of 300 bursts with an amplitude of 250 V/cm. Each burst consisted of 200 pulses with a duration of 850 ns for a total on-time of 170 µs. Relative to the size of the brain, the volume of BBB disruption was substantial (0.51 $cm^3$). Other than physical damage due to the electrode insertion, there was no noticeable neuroinflammation or cell death when capase-3 activity from Group 1 was compared to Group 6 controls or the unoperated control. It is important to note that cell morphologic criteria were used to define dead cells and caspase-3 was used to corroborate those findings. Future work should include later time points to investigate the possibility of delayed effects and the reversibility of the BBB disruption.

As the number of bursts containing 500 ns pulses (programmed) was increased (Groups 2 and 3), evidence of cell death was noted by cytoplasmic condensation, nuclear pyknosis, and apoptotic body formation. The same is true when the individual pulse duration was increased to 2 µs, while programming the same on-time (Group 4). Interestingly, Group 3 exhibited markedly greater caspase-3 activity than Group 4. We hypothesize that this effect could be due to the ability of sub-microsecond pulses to exert greater influence on intracellular structures[23,24]. Overall, increasing the number of bursts above 600, or increasing the programmed pulse duration above 500 ns did not significantly alter the volume of BBB disruption. This suggests that the effect has reached a plateau, and additional energy is deleterious to cell viability. In Group 5, necrosis was evident without a significant increase in caspase-3 expression. This finding is comparable to that found by Rossmeisl *et al.*, where unipolar IRE pulses applied at similar electric fields caused no significant or specific immunoreactivity to Bcl-2, caspase-3, or caspase-9 within the lesions[25].

The dissipated energy density for each treatment (**Table 2**) can be calculated by:

$$U = \sigma |E|^2 t \tag{2}$$

where $\sigma$ is the conductivity of the tissue, $E$ is the electric field, and $t$ is the total energized time (burst on-time × number of bursts). The conductivity was estimated to be 0.18 S/m according to data generated by Gabriel *et al.* for gray matter at 1 MHz[26]. Assuming a perfectly insulative unitary volume, the temperature change can then be estimated according to:

$$\Delta T = \frac{U}{\rho c} \tag{3}$$

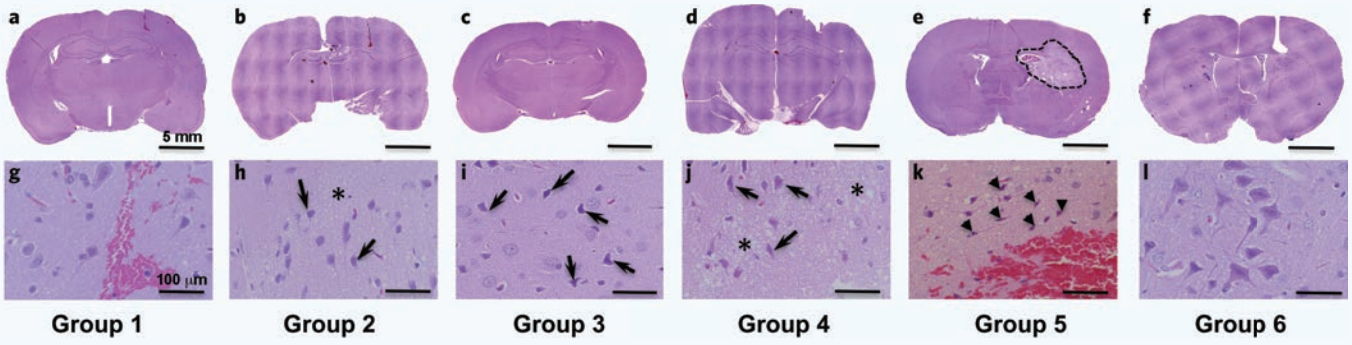


**Figure 4** Histological assessment following VEIN pulse treatment. In Groups 1 (**a,** caudal electrode) and 6 (**f,** rostral electrode), brain damage is confined to the electrode insertion tracks with preservation of the cellular morphology in surrounding treated regions (**g,l**). In Groups 2 (**b,h**), 3 (**c,i**), and 4 (**d,j**), varying degrees of cellular condensation and nuclear pyknosis (**h,i,j,** arrows) and regional vacuolization of the neurophil (**h,j,***) were observed in treated regions. Complete loss of normal cerebral cytoarchitecture (**e,** broken line), associated with parenchyhmal hemorrhage and neuronal necrosis (**k,** arrowheads) around the rostral electrode in Group 5. All sections stained with hematoxylin and eosin. Bars = 5 mm in top panels, and 100 µm in bottom panels.

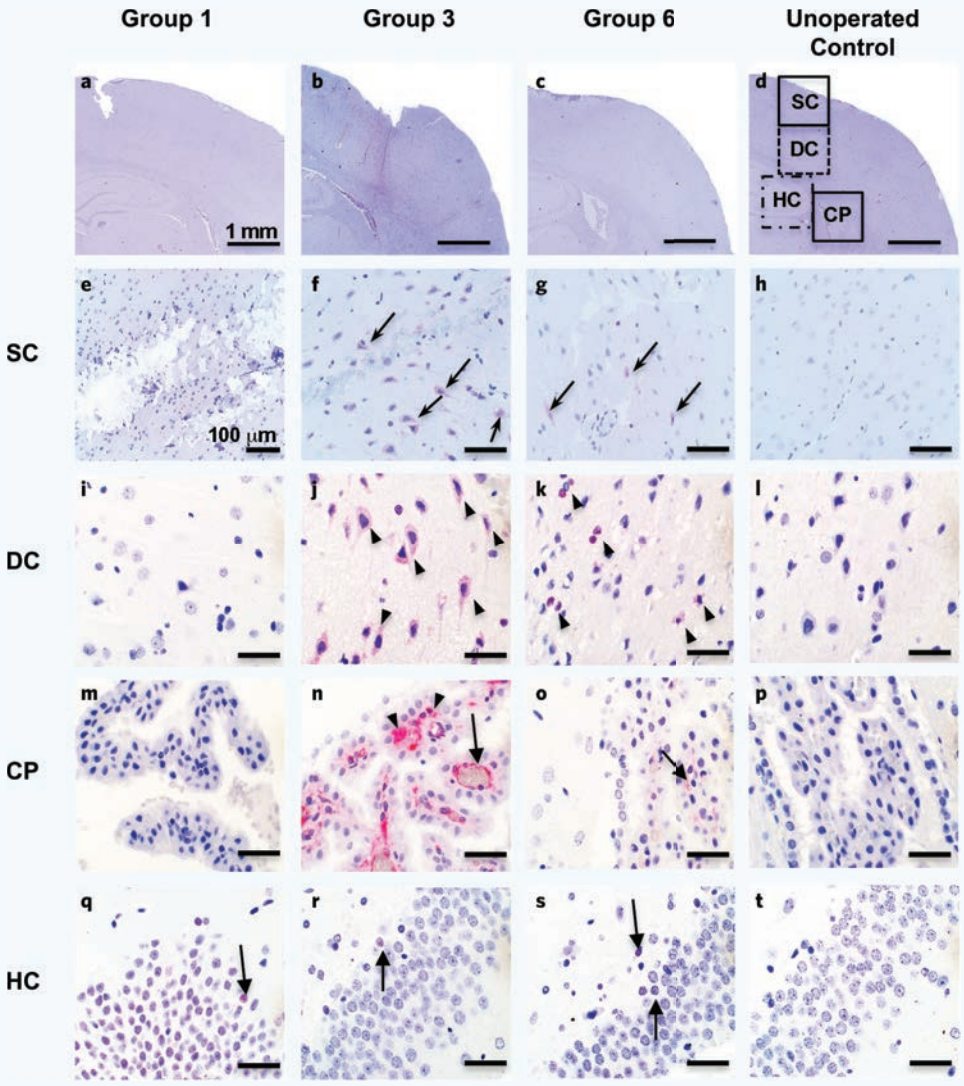


**Figure 5** Qualitative caspase-3 immunohistochemistry in Groups 1, 3, 6, and unoperated controls. In Groups 1 (**a**) and the unoperated controls (**d**), caspase-3 immunoreactivity was rarely observed in neurons within the superficial cortex (SC), deep cerebral cortex (DC), or choroid plexus (CP) epithelium and endothelium. In Group 3 (**b**), marked caspase-3 immunoreactivity was observed in the SC (**f,** arrows), CP plexus endothelium (**n,** thin arrow) and epithelium (**n,** arrowhead), and DC (**j,** arrowheads) within neurons adjacent to the electrode track. In Group 6 (**c**), caspase-3 positive neurons were also observed in the SC (**g,** arrows) and DC (**k,** arrowheads) regions as well as in the CP endothelium (**o,** thin arrow). In panel **d,** the boxes indicate SC, DC, CP, and HC (hippocampus) regions from which RFV were selected for quantitative caspase-3 analyses. Occasional immunoreactive HC neurons were observed in all Groups (**q–t,** thin arrows). Bars = 1 mm in panels **a–d,** and 100 µm in all other panels.

where $\rho$ and $c$ are the density and specific heat capacity of the tissue, respectively. These values are chosen to be the same as water ($\rho = 4.184$ J/(gK), $c = 1 \times 10^6$ g/m$^3$). For comparison, the calculations were also made for an IRE treatment, in which it was shown that thermal effects were negligible. From this comparison, we conclude that the effects seen in Groups 1 through 4 were non-thermal in nature. The comparatively higher energy delivery in Group 5 resulted in thermal damage, including coagulative necrosis near the electrodes where the electric field is elevated. However, these temperature predictions are conservative in that they assume the entire tissue is uniformly exposed to the electric field, and they do not account for heat dissipation between the pulses and heat convection from the surface of the tissue. Future work should include monitoring of temperature during treatment to confirm the predictions.

Reversible electroporation combined with chemotherapeutic agents, or electrochemotherapy, has proven to be effective in treating brain tumors in a rat model with minimal side effects[27,28]. In this pre-clinical work, the chemotherapeutic agent bleomycin was administered directly into the tumor before applying electric pulses, which circumvented the BBB. It was later noted that a potential usage of electrochemotherapy could be to treat the infiltrative margins of a tumor after surgical debulking[29], as those regions are well-vascularized with an intact BBB. In a study conducted by Hjouj *et al.*, BBB disruption was evaluated for 50 to 90 unipolar pulses as short as 50 µs[30]. When the pulse amplitude was between 330 V/cm and 500 V/cm, it was concluded that transient BBB disruption without permanent tissue damage was the result of reversible electroporation. This is similar to the finding in Ref. 18 that electroporation is predominantly reversible at electric field strengths below 400 V/cm in normal brain.

Here, BBB disruption is observed at an even lower electric field (250 V/cm) when a greater number of bipolar bursts are applied. Therefore, it is feasible that the mechanism of opening the BBB does not rely completely on reversible electroporation. One possible explanation is that the presence of tight junctions increases the transendothelial electrical resistance of the BBB[31]. As a result, there is a large voltage drop across the endothelial cells, and it is possible that even low voltages produce high electric fields that compromise the integrity of tight junctional proteins. BBB disruption without electroporation has been shown *in vitro* when performing protocols for deep brain stimulation across endothelial cell monolayers[32]. The waveforms were bipolar with individual pulse durations of 90 µs, and they were applied continuously for 5 minutes at 2.5 V/cm. The *in vivo* microscopic electric field distribution is complicated, and one cannot rule out the possibility of other explanations, including low level heating due to the high electrical conductivity of the blood, without further experimentation.

Researchers have investigated BBB disruption as a health hazard in response to electromagnetic radiation[33]. When 200, 14 ns pulses were applied at 2000 V/cm, increased BBB permeability was noted along with altered localization and decreased levels of the tight junctional protein ZO-1. Magnetic fields have also been used to disrupt the BBB when

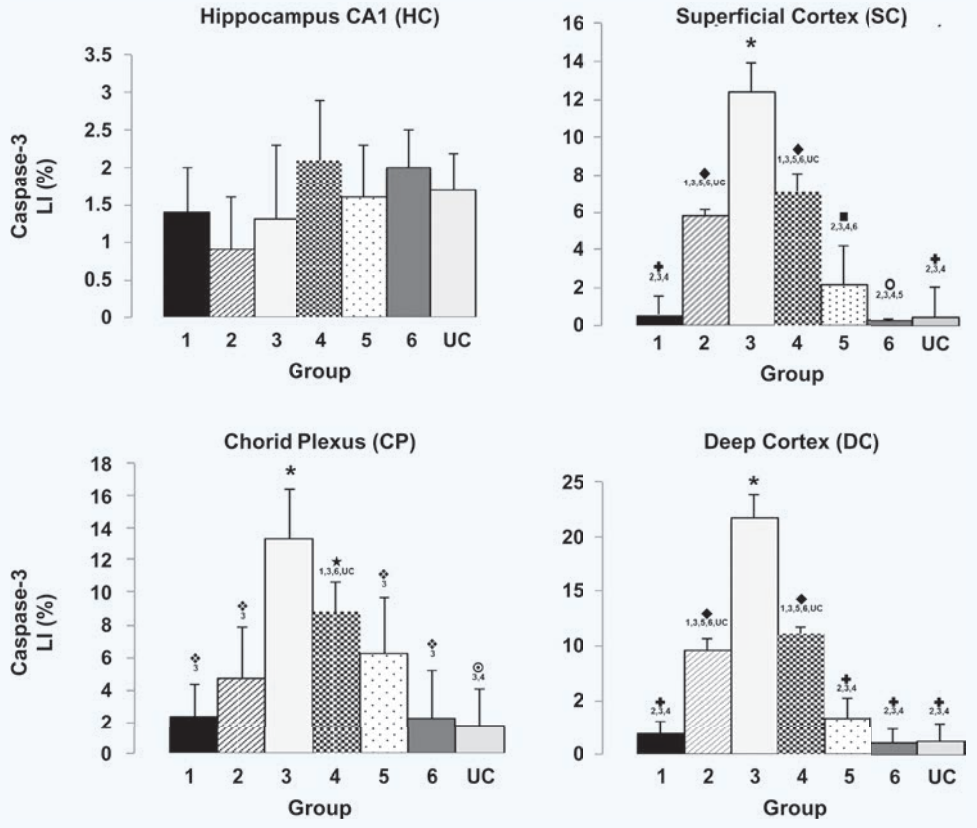


**Figure 6** Quantitative caspase-3 labeling indices (LI) for all groups and brain regions. Symbols indicate significant ($p < 0.05$) difference from labeled group from numerically designated groups under symbol. Asterisk (*) denotes significant difference in labeled group ($p < 0.05$) from all other groups. UC = unoperated control.

combined with magnetic nanoparticles. In the presence of an alternating magnetic field, the iron oxide nanoparticles release heat and cause localized hyperthermia (≥ 38°C for 30 minutes) that is thought to transiently open the BBB[34]. These particles can also be steered to the target location using magnetic resonance. Additionally, activation of photosensitizing agents with laser light (600–700 nm) has been shown to disrupt tumor vasculature[22,35]. This affect can also be targeted to the BBB and reversible at low fluence levels (9 J)[35].

Even at the highest energy setting (Group 5), no muscle contractions were observed. This serves as confirmation of our previous results, which show that bipolar pulses reduce the electric field threshold for stimulating an action potential[21]. When very short pulses are used, there is a latency period between the offset of the pulse and the rising phase of the action potential. Reversing the pulse polarity within the latency period can inhibit action potential generation[36]. An additional benefit to very short, bipolar pulses, it that they have the potential to create more uniform treatment volumes within heterogeneous tissues[37]. This could prove beneficial in treatment planning for tumor ablation and BBB disruption, as the brain is composed of multiple tissue types with varying electrical properties.

## CONCLUSION

The VEIN pulse platform is a feasible technique for performing sub-lethal BBB disruption. The results presented herein warrant future studies directed at optimizing the range of effective pulse parameters and exploring the exact mechanism of action. If translated clinically, this treatment has the potential to enhance drug delivery in the brain for treating a wide range of disease including brain cancer, Parkinson's disease, and Alzheimer's disease. Additionally, with respect to brain cancer, there is the option of performing a combinatorial technique that relies on an initial set of lethal pulse parameters to destroy the primary tumor followed by a sub-lethal set of pulse parameters to improve drug diffusion to the infiltrative cells beyond the tumor margin.

## ACKNOWLEDGEMENTS

This work was supported by the Golfers Against Cancer, the Center for Biomolecular Imaging in the Wake Forest School of Medicine, the NSF CAREER Award CBET-1055913, and the NSF I-Corps Award 1265105. C.B.A. acknowledges the NIGMS division of Training, Workforce Development, and Diversity under the IRACDA grant #K12-GM000678. The authors thank Dana Calicott and John Robertson for their assistance with the animal procedures, and Yong Woo Lee for his valuable contributions in designing the experiments.

## REFERENCES

1. La Rocca, R.V. & Mehdorn, H.M. Localized BCNU chemotherapy and the multimodal management of malignant glioma. *Curr. Med. Res. Opin.* **25**(1), 149–160 (2009).
2. Stupp, R. *et al*. Radiotherapy plus concomitant and adjuvant temozolomide for glioblastoma. *N. Engl. J. Med.* **352**(10), 987–996 (2005).
3. Holland, E.C. Glioblastoma multiforme: The terminator. *Proc. Natl. Acad. Sci. USA* **97**(12), 6242–6244 (2000).
4. Stoica, G. *et al*. Morphology, immunohistochemistry, and genetic alterations in dog astrocytomas, *Vet. Pathol.* **41**(1), 10–19 (2004).
5. Barajas, R.F., Jr. *et al*. Regional variation in histopathologic features of tumor specimens from treatment-naive glioblastoma correlates with anatomic and physiologic MR imaging. *Neurol. Oncol.* **14**(7), 942–954 (2012).
6. Saraswathy, S. *et al*. Evaluation of MR markers that predict survival in patients with newly diagnosed GBM prior to adjuvant therapy. *J. Neuro-Oncol.* **91**(1), 69–81 (2009).
7. Liu, H.L. *et al*. Blood-brain barrier disruption with focused ultrasound enhances delivery of chemotherapeutic drugs for glioblastoma treatment. *Radiology* **255**(2), 415–425 (2010).
8. Angelov, L. *et al*. Blood-brain barrier disruption and intra-arterial methotrexate-based therapy for newly diagnosed primary CNS lymphoma: A multi-institutional experience. *J. Clin. Oncol.* **27**(21), 3503–3509 (2009).
9. Alyautdin, R. *et al*. Nanoscale drug delivery systems and the blood-brain barrier. *Int. J. Nanomed.* **9**, 795–811 (2014).
10. Warren, K. *et al*. Phase II trial of intravenous lobradimil and carboplatin in childhood brain tumors: A report from the Children's Oncology Group. *Cancer Chemother. Pharmacol.* **58**(3), 343–347 (2006).
11. Hynynen, K. *et al*. Noninvasive MR imaging-guided focal opening of the blood-brain barrier in rabbits. *Radiology* **220**(3), 640–646 (2001).
12. Sheikov, N. *et al*. Cellular mechanisms of the blood-brain barrier opening induced by ultrasound in presence of microbubbles, *Ultrasound Med. Biol.* **30**(7), 979–989 (2004).
13. Zhou, Y.F. High intensity focused ultrasound in clinical tumor ablation, *World J. Clin. Oncol.* **2**(1), 8–27 (2011).
14. Davalos, R.V., Mir, L.M. & Rubinsky, B. Tissue ablation with irreversible electroporation. *Ann. Biomed. Eng.* **33**(2), 223–231 (2005).
15. Davalos, R.V., Rubinsky, B. & Mir, L.M. Theoretical analysis of the thermal effects during *in vivo* tissue electroporation, *Bioelectrochemistry* **61**(1–2), 99–107 (2003).

16. Garcia, P.A. *et al*. Non-thermal irreversible electroporation (N-TIRE) and adjuvant fractionated radiotherapeutic multimodal therapy for intracranial malignant glioma in a canine patient, *Technol. Cancer Res. Treat.* **10**(1), 73–83 (2011).
17. Garcia, P. *et al*. Nonthermal irreversible electroporation as a focal ablation treatment for brain cancer. In *Tumors of the Central Nervous System,* Volume 12 (ed.) Hayat, M.A. (Springer, Netherlands, 2014), pp. 171–182.
18. Garcia, P.A. *et al*. 7.0-T magnetic resonance imaging characterization of acute blood-brain-barrier disruption achieved with intracranial irreversible electroporation. *PloS One.* **7**(11), e50482 (2012).
19. Ellis, T.L. *et al*. Nonthermal irreversible electroporation for intracranial surgical applications. Laboratory investigation. *J. Neurosurg*. **114**(3), 681–688 (2011).
20. Arena, C.B. & Davalos, R.V. Advances in therapeutic electroporation to mitigate muscle contractions. *J. Membrane Sci. Technol*. **2,** e102 (2012).
21. Arena, C.B. *et al*. High-frequency irreversible electroporation (H-FIRE) for non-thermal ablation without muscle contraction. *Biomed. Eng. Online* **10**(1), 102 (2011).
22. Chen, B. *et al*. Tumor vascular permeabilization by vascular-targeting photosensitization: Effects, mechanism, and therapeutic implications. *Clin. Cancer Res*. **12**(3 Pt 1), 917–923 (2006).
23. Beebe, S.J. *et al*. Nanosecond, high-intensity pulsed electric fields induce apoptosis in human cells. *FASEB J*. **17**(11), 1493–1495 (2003).
24. Weaver, J.C. *et al*. A brief overview of electroporation pulse strength-duration space: A region where additional intracellular effects are expected, *Bioelectrochemistry* **87**, 236–243 (2012).
25. Rossmeisl, J.H., Jr. *et al*. Pathology of non-thermal irreversible electroporation (N-TIRE)-induced ablation of the canine brain. *J. Vet. Sci*. **14**(4), 433–440 (2013).
26. Gabriel, C. & Gabriel, S. *Compilation of the Dielectric Properties of Body Tissues at RF and Microwave Frequencies*. Occupational and Environmental Health Directorate, Radiofrequency Radiation Division, Brooks Air Force Base (Physics Department, King's College London, 1997).
27. Agerholm-Larsen, B. *et al*. Preclinical Validation of electrochemotherapy as an effective treatment for brain tumors. *Cancer Res*. **71**(11), 3753–3762 (2011).
28. Salford, L.G. *et al*. A new brain tumour therapy combining bleomycin with *in vivo* electropermeabilization. *Biochem. Biophys. Res. Commun*. **194**(2), 938–943 (1993).
29. Linnert, M. *et al*. Treatment of brain tumors: Electrochemotherapy. In *Tumors of the Central Nervous System,* Volume 12 (ed.) Hayat, M.A. (Springer, Netherlands, 2014), pp. 247–259.
30. Hjouj, M. *et al*. MRI study on reversible and irreversible electroporation induced blood brain barrier disruption, *PloS One* **7**(8), e42817 (2012).
31. Wolburg, H. & Lippoldt, A. Tight junctions of the blood-brain barrier: Development, composition and regulation. *Vascul. Pharmacol*. **38**(6), 323–337 (2002).
32. Lopez-Quintero, S.V. *et al*. DBS-relevant electric fields increase hydraulic conductivity of *in vitro* endothelial monolayers. *J. Neural Eng*. **7**(1), 16005 (2010).
33. Ding, G.R. *et al*. EMP-induced alterations of tight junction protein expression and disruption of the blood-brain barrier. *Toxicol. Lett*. **196**(3), 154–160 (2010).
34. Tabatabaei, S.N. *et al*. Towards MR-navigable nanorobotic carriers for drug delivery into the brain, *IEEE Int. Conf. Robot. Autom.* **May 14**, 727–732 (2012).
35. Hirschberg, H. *et al*. Disruption of the blood-brain barrier following ALA-mediated photodynamic therapy. *Lasers Surg. Med*. **40**(8), 535–542 (2008).
36. van den Honert, C. Mortimer, J.T. Response of the myelinated nerve fiber to short duration biphasic stimulating currents. *Ann. Biomed. Eng*. **7**(2), 117–125 (1979).
37. Arena, C.B., *et al*. Theoretical considerations of tissue electroporation with high-frequency bipolar pulses. *IEEE Trans. Biomed. Eng*. **58**(5), 1474–1482 (2011).